analytical chemistry

pubs.acs.org/ac
Article

Simply Designed and Universal DNA Nanohydrogel for Stimuli-Responsive NIR-II Fluorescence Imaging of Early-Stage Tumor

Feng Gao,[⊥] Lichao Guo,[⊥] Wanjuan Lin, Xiaobo Zhang, Qichen Zhan,* Peng Cao,* Huangxian Ju,* and Yue Zhang*

Cite This: *Anal. Chem.* 2025, 97, 10699−10708
Read Online

ABSTRACT: The delayed detection and recurrence of cancer lead to disappointing cure rates, underscoring the imperative for exploring precise early tumor diagnosis techniques. Despite the superior biocompatibility and flexible programmability of DNA nanoprobes for tumor imaging, intricate designs with multiple oligonucleotide sequences are always indispensable, which significantly hinder their clinical application and commercial development. To construct a simply designed DNA nanoprobe, here, we constructed a universal stimuli-responsive nanohydrogel through the hybridization of the staple strand and skeleton strand. Through a simple substitution of the staple strand, this hydrogel can be adapted for the response to different targets without necessitating a series of subsequent revisions and synthesis optimization. To achieve near-infrared II region (NIR-II) fluorescence imaging, alkynyl-modified NIR-II fluorescent dyes are labeled at two ends of bent staple strands and display weak fluorescence because of the aggregation-caused quenching effect. The highly expressed ATP or cytokine in tumor cells activates the liberation of staples and collapse of the bent configuration, which generates fluorescence recovery for tumor imaging. Moreover, this nanohydrogel also allows for the targeted release of anticancer drugs intercalated in the DNA helix. By integration of NIR-II fluorescent dyes, this versatile nanohydrogel enables precise diagnosis and treatment of early tumors. The straightforward design demonstrates low cost and easy adaptability for multitarget detection, highlighting its significant implications for the advancement of DNA nanotechnology in clinical application and commercialization production.

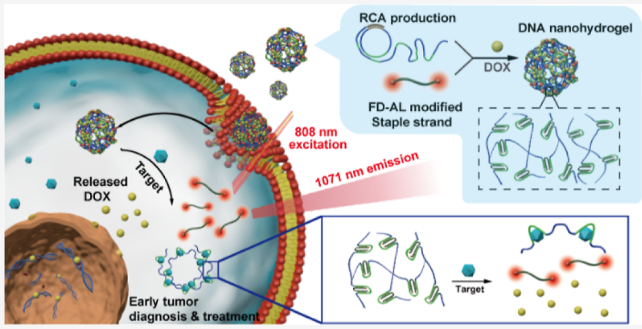

INTRODUCTION

At present, cancer stands as one of the most significant health concerns in global terms, posing a formidable threat to public health. Despite the development of various therapeutic interventions, delayed detection and cancer recurrence lead to low cure rates and elevated lethality. Thus, exploring precise tumor imaging techniques for early tumor diagnosis and sensitive detection holds great significance for enhancing cancer therapy and improving patient prognosis. Compared with normal tissues, tumor tissues present quite different characteristics including lower pH,[1,2] hypoxic environment,[3] enhanced expressions of GSH,[4] higher concentration of H_2O_2,[5,6] and raised level of ATP.[7] Taking advantage of these unique properties of tumors, various responsive fluorescent nanoprobes based on DNA nanotechnology, organometallic frameworks, or polymer materials have been developed for tumor-specific detection and imaging.[8]

Although fluorescence imaging possesses benefits including high sensitivity and resolution, non-invasion, and multiplexing,[9] conventional fluorescence detection suffers low penetration depth and severe background interference, which are lethal for analysis of complex biological systems and create obstacles for deep tumor imaging.[10] In contrast, the long wavelength of second near-infrared (NIR-II) light confers superior fluorescence penetration, with diminished biological background signals, thereby augmenting the signal-to-noise ratio for in vivo imaging applications.[11] Recently, more and more NIR-II fluorescent materials have been discovered to achieve high-resolution bioimaging, such as quantum dots,[12] small-molecule dyes,[13] rare-earth nanoparticles,[14−16] and carbon nanotubes.[17] In addition, metal-based chemical agents such as Pt(II) metallacycle[18,19] and Ru(II) metallacycle[20] with enhanced phototherapy activity offer emerging opportunities for fluorescent materials for in vivo biomedical applications.

Organic small-molecule dyes with NIR-II fluorescence properties have great potential for bioimaging considering their well-defined structures, good optical properties, and easy

Received: January 24, 2025
Revised: May 7, 2025
Accepted: May 7, 2025
Published: May 13, 2025

https://doi.org/10.1021/acs.analchem.5c00581
Anal. Chem. 2025, 97, 10699−10708

Scheme 1. Illustration of (A) the Synthesis of DOX-Loaded DNA Nanohydrogel and (B) ATP-Responsive NIR-II Fluorescent Tumor Imaging and Therapy

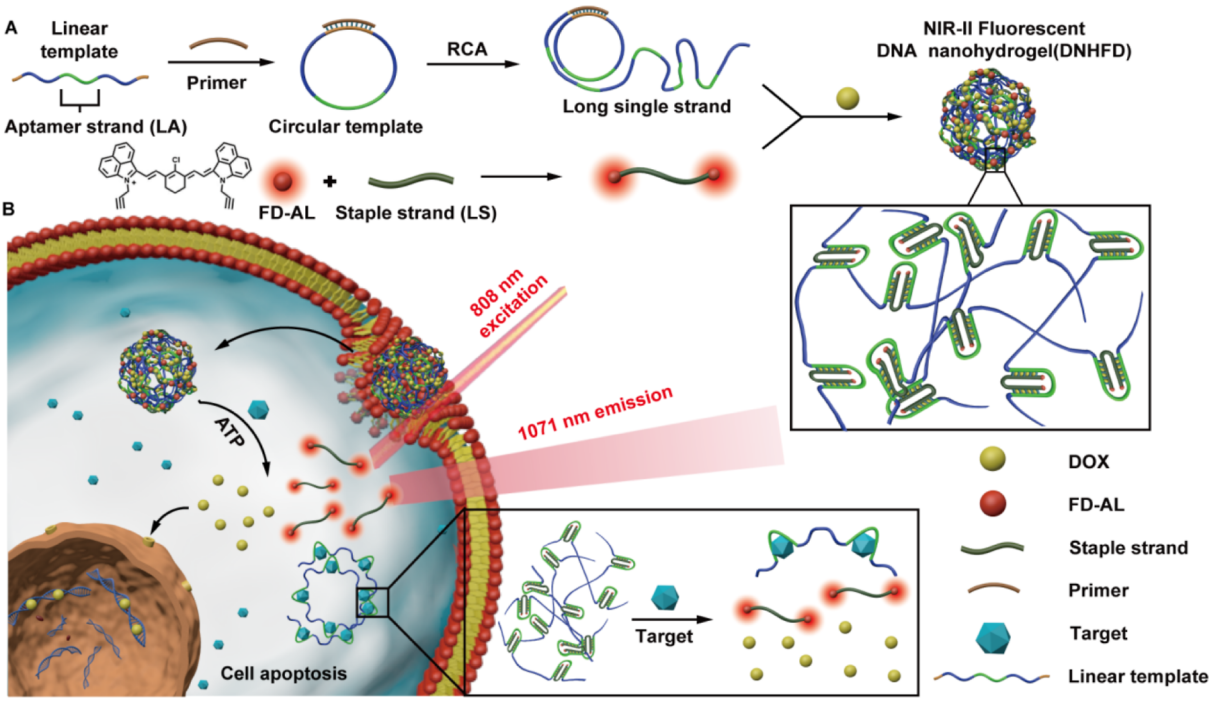

metabolism. But their lower cell uptake rate and the deficiency of targeted accumulation hinder the application in tumor imaging and diagnosis. Therefore, various nanocarriers for loading dyes have been designed to improve the ability of tumor accumulation in vivo, such as polymeric micelles,[21] metal−organic frameworks,[22−24] and silica nanoparticles.[25] As a kind of natural biological material, DNA nanomaterials have the advantages of superior biocompatibility and biodegradability and low toxicity and thus have gained popularity in biomedical applications.[26] Besides, their inherent flexibility in programmability and deformability enables convenient construction of stimuli-responsive detection probes for multiple biomarkers.[27]

However, most DNA nanoprobes involve multiple oligonucleotide sequences, which brings complexity to the target-responsive design and higher cost, posing negligible obstacles for their clinical applications and commercialized manufacture. Therefore, there is a pressing demand to develop a simple, versatile DNA nanoprobe with a low cost for clinical tumor imaging as a convenient method for preparing long single DNA strands with repetitive units, relatively low cost, easy operation, and mild reaction conditions.[26−28] Through integration with functional nucleic acids such as aptamers, i-motif structures, and G-quadruplexes,[29−31] diversiform stimuli-responsive DNA nanostructures could be created for the precise imaging and diagnosis of early tumors in vivo.[32] Based on the RCA reaction, we constructed a simply designed and universal DNA nanohydrogel to achieve the stimuli-responsive regulation of NIR-II fluorescent dyes for deep tumor imaging.

Considering the high expression of ATP in the tumor cells, an ATP-triggered nanohydrogel was first designed, in which the circular template strand containing the ATP aptamer sequence (green section in Scheme 1A) was synthesized to obtain a long single strand of DNA with repetitive aptamer sequences (LA) by RCA reaction. Then, the staple DNA strand (LS) partially hybridized with LA to fold the long single strand, thus facilitating the formation of DNA nanohydrogel (DNH) (Scheme 1). The bent configuration brought the adjacency of two fluorescent dyes (FD-AL) modified at the LS terminal, inducing the NIR-II fluorescence quenching of FD-AL. The combination of ATP with the aptamer sequences broke off the assembly of nanohydrogel and induced the separation of FD-AL molecules from each other, recovering fluorescence at 1071 nm under 808 nm excitation. To evaluate the versatility of this platform, the anticancer drug doxorubicin (DOX) was loaded in a DNA double helix and liberated after disassembly of DNH for tumor cell killing. Moreover, interferon-gamma (INF-γ)-responsive nanohydrogel was also constructed, indicating the superior adaptability to different targets of this design. Through the low-cost synthesis and simple sequence design, this DNA nanohydrogel demonstrates significant implications for the clinical application and commercialization of DNA nanotechnology.

RESULTS AND DISCUSSION

ATP-Induced Conformational Variation. ATP stands out as a pivotal biomarker for tumor diagnosis.[28] Therefore, we leveraged the ATP aptamer as the specific signal response module to achieve precise and targeted imaging of tumors in vivo. First, the ATP aptamer's ability to recognize and selectively bind to ATP was experimentally validated using polyacrylamide gel electrophoresis (PAGE). As shown in Figure S1, after incubating the ATP aptamer with the lock strand that contained complementary sequences, a band with a much lower migration rate could be observed in lane 3, indicating the hybridization of these two DNA strands. Then, the ATP-responsive disassembly of this coalition was verified through PAGE imaging after adding ATP with different concentrations. As the concentration of ATP increased (1 μM, 3 μM, 5 μM), two bands of single ATP aptamer and lock

https://doi.org/10.1021/acs.analchem.5c00581
Anal. Chem. 2025, 97, 10699−10708

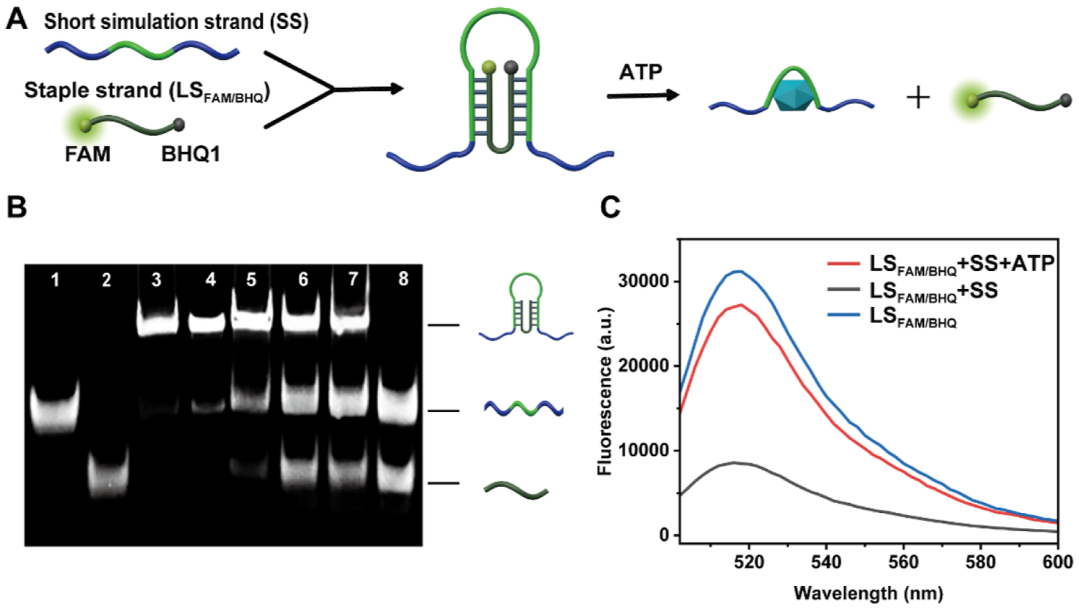

Figure 1. Recognition and combination with ATP. (A) Illustration of DNA strand folding and ATP-responsive unwinding. (B) PAGE analysis of staple strand (LS) release after incubation with different concentrations of ATP. Lanes 1−8 represent the short simulation strand (I), staple strand (II), mixture of I and II, and then that treated with 0, 1, 5, 10, 50, and 100 μM ATP. (C) Fluorescence spectra of the initial LS$_{FAM/BHQ}$, LS$_{FAM/BHQ}$ incubated with short simulation strand (SS), and then that incubated with ATP.

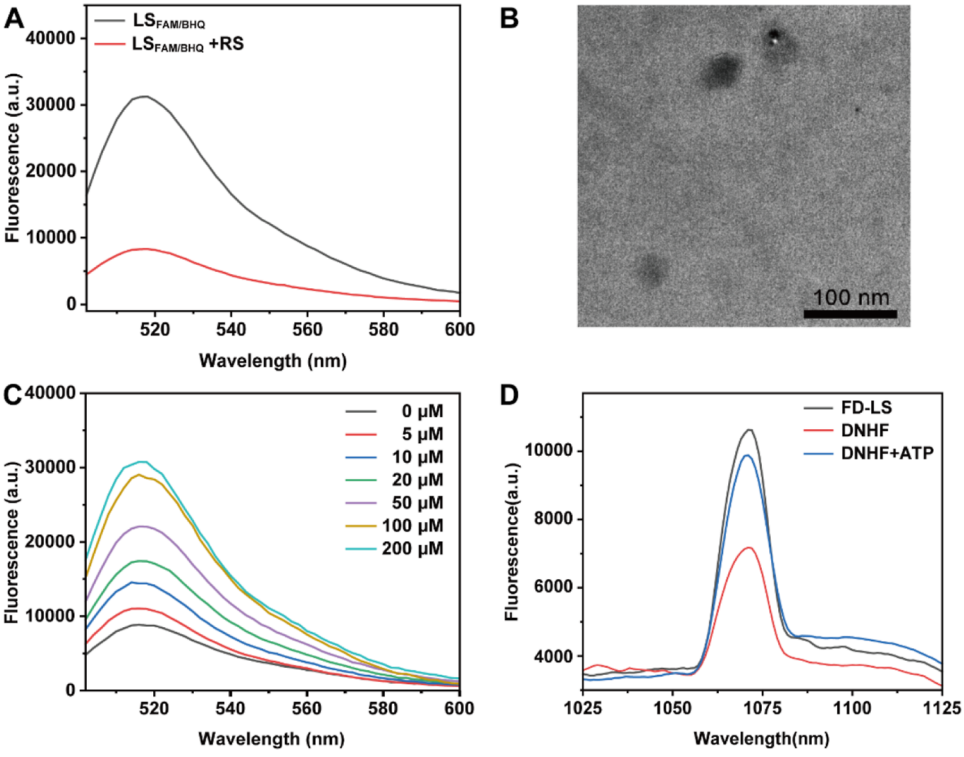

Figure 2. Formation of DNA nanohydrogel and ATP-responsive collapse. (A) Fluorescence spectra of LS$_{FAM/BHQ}$ before and after incubation with the RCA production (RS). (B) TEM image of DNA nanohydrogel. (C) Fluorescence spectra of DNA nanohydrogel treated with different concentrations of ATP. (D) NIR-II fluorescence spectra of FD-AL-modified staple strand (FD-LS) and DNHF synthesized from FD-LS before and after treatment with ATP.

strand became more discernible with higher brightness (Figure S1, lanes 4, 5, and 6), indicating successful combination of ATP with the aptamer and the ATP-responsive disintegration of this double helix configuration.

In order to form a bent configuration, a staple DNA strand (LS) was designed with complementary fragments at 5′ as well as 3′ ends to hybridize with the ATP aptamer sequences in the long strand (Figure 1A). The ATP-induced strand displacement was verified by PAGE and fluorescence detection. First, a short simulation stand with the same sequence of the repeated sequence in RCA production was used to explore the ATP-induced disassembly. As shown in Figure 1B, the band of lane

https://doi.org/10.1021/acs.analchem.5c00581
Anal. Chem. 2025, 97, 10699−10708

3 with much lower migration indicated that the short simulation chain containing the ATP aptamer hybridized with the staple DNA strand to create a new band, while this assembly gradually collapsed and generated two bands of short simulation chain and LS with the increasing concentration of ATP. When the concentration reached 100 μM, the chain was completely unwound, and the experimental results showed that even the short simulation chain had a good ATP-responsive unwinding. We then verified the conformational variation through fluorescence changes. As shown in Figure 1C, the LS chain labeled with FAM and BHQ1 ($LS_{FAM/BHQ}$) showed intense fluorescence intensity of FAM (Figure 1C, blue line), which experienced a notable decrease following the hybridization with the short simulation chain because of the adjacency of FAM and quenching BHQ1, indicating the formation of a bent conformation. When ATP was added, the fluorescence signal of FAM exhibited an obvious recovery (Figure 1C, red line), which further suggested ATP-induced disintegration of the bent configuration. The above results demonstrate the folded conformation and ATP responsiveness of the LS chain linked to the short simulation strand.

Considering that the length of the complementary section between the short simulation chain and the staple strand might affect the hybridization efficiency and ATP responsiveness, we optimized their complementary base number through fluorescence signal variation. As shown in Figure S2A,B, an optimal fluorescence signal-to-noise ratio was achieved when the number of complementary bases reached 10, which guided our choice of the short simulation chain and staple strand with 10 complementary bases as the most suitable candidate for subsequent experimental investigations and further characterization.

Synthesis and Characterization of Stimuli-Responsive DNA Nanohydrogels. The RCA reaction was performed using the template strand to synthesize a long single-stranded structure with repetitive sequences, including ATP aptamer sequences (Figure S3A), which was verified by PAGE imaging. First, a circular template was obtained through incubating the template strand with the linkage strand. After treatment with Exo I/III to degrade excess unreacted linear oligonucleotides, a single band could be observed (Figure S3B, lane 3), implying the successful generation of a DNA circle for subsequent reaction. Afterwards, the production of long single strands was also verified through PAGE. After mixing the circular template (Figure S3B, lane 3) with primer DNA (Figure S3B, lane 4) for the RCA reaction, a band with a much lower migration rate could be observed (Figure S3B, lane 5) under the amplification of phi29 DNA polymerase, indicating the successful RCA reaction and generation of a long DNA strand.

The staple strands hybridized with the repeated sequences in the obtained long single strand, inducing multiple folding transformations and ultimately leading to the formation of a compact globular structure. The bent configuration of staple strands was verified through the fluorescence quenching of $LS_{FAM/BHQ}$, which presented an obvious decrease in FAM fluorescence intensity after the reaction of the LS chain with the RCA long single chain (Figure 2A), indicating the formation of the folded structure. Then, the formed globular nanostructures were further characterized by transmission electron microscopy (TEM) and dynamic light scattering (DLS). The hydration diameter of this DNA nanohydrogel was measured to be around 50 nm according to DLS analysis (Figure S4), and the monodisperse particle size in the TEM image is about 40 nm (Figure 2B). Moreover, atomic force microscopy (AFM) characterization was also conducted to evaluate the morphology and height of this DNA nanohydrogel, which demonstrated uniform size around 42 nm and height around 12 nm (Figure S5). These results indicate that the long single chain obtained from RCA could transform into a spherical nanostructure through hybridization with staple strands.

Self-quenched DNA nanohydrogel was synthesized using $LB_{FAM/BHQ}$ to verify that ATP could break up the assembly of DNH. The fluorescence recovery of FAM was monitored after incubation with different concentrations of ATP, which displayed a significant increase in the fluorescence intensity of FAM as the concentration of ATP rose (Figure 2C), demonstrating the liberation of $LB_{FAM/BHQ}$ from the RCA skeleton and the collapse of the DNA nanohydrogel.

To demonstrate the versatile adaptability of this nanohydrogel to various targets, a long single strand with repeated INF-γ aptamer fragments was synthesized and incubated with the complementary staple strands. DLS characterization revealed that the long strands containing the INF-γ aptamers underwent bending and compacted assembly into nanohydrogels with a hydration diameter of approximately 49 nm (Figure S6A). Furthermore, the responsiveness to INF-γ was confirmed through fluorescence assays using Cy3 and BHQ2 conjugated staple strands. As shown in Figure S6B, significant fluorescence quenching could be observed following assembly with the RCA-generated long strand, while upon the addition of INF-γ, the fluorescence signal of Cy3 was recovered because of the disintegration of the bending configuration, demonstrating the straightforward design and superior responsiveness to diverse targets of this DNA nanohydrogel.

ATP-Responsive NIR-II Fluorescence of DNA Nanohydrogel. To achieve targeted NIR-II fluorescence tumor imaging, a commonly used dye, FD-1080, with excellent NIR-II fluorescent properties was chosen as a fluorescent element in the design of DNA nanohydrogel.[29] Considering the deficiency and dilemma of FD-1080 for conjugation with macromolecular polymers, we synthesized the alkyne-modified probe (FD-AL) through a four-step reaction, which is described in Figure S7 and characterized through ^{1}H NMR, ^{1}C NMR, and high-resolution mass spectrum (Figures S8−S19). After covalent linkage with the azide-labeled LS strand through the click reaction, the FD-AL-modified LS (FD-LS) showed the same characteristic emission peak at 1071 nm as that of FD-AL under 808 nm excitation (Figure S20), indicating the successful modification of NIR-II fluorescent FD-AL to the DNA strand. After assembly with the long single strand to form a compressed spherical structure, the fluorescence intensity at 1071 nm was restrained because of the aggregation quenching effect[30] (Figure 2D, red line) in comparison with the original FD-LS (Figure 2D, red line). However, in the presence of ATP, the formed FD-AL-modified DNA nanohydrogel (DNHF) collapsed and displayed a recovered NIR-II fluorescence signal (Figure 2D, blue line) under the recognition and combination with ATP, indicating the potential to achieve ATP-responsive NIR-II tumor imaging of this nanohydrogel.

Loading and ATP-Responsive Release of DOX. In order to achieve drug delivery and controlled release for accurate tumor therapy, the anticancer drug DOX (doxorubicin) was loaded into DNHF through intercalation of DOX

https://doi.org/10.1021/acs.analchem.5c00581
Anal. Chem. 2025, 97, 10699−10708

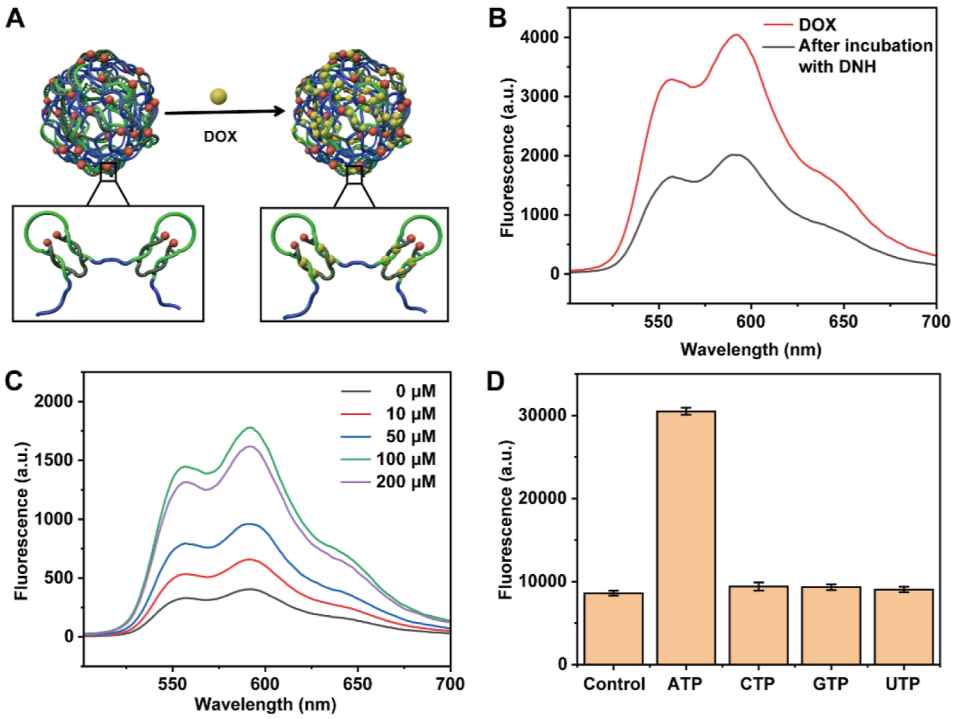

Figure 3. DOX loading and ATP-responsive release. (A) Illustration of DOX loading into DNA nanohydrogel through intercalation. (B) Fluorescence spectra of DOX in the supernatant before and after incubation with DNA nanohydrogel. (C) Fluorescence spectra of the supernatants after incubating the DOX-loaded DNA nanohydrogel with different concentrations of ATP. (D) The DOX fluorescence intensity of the supernatants after incubating the DOX-loaded DNA nanohydrogel with ATP, CTP, GTP, or UTP. The data error bars indicate means ± SD (n = 3).

into the DNA double helix structure (Figure 3A).[31] As shown in Figure 3B, the successful loading of DOX was verified through detection of the fluorescence variation of DOX. After incubating DNHF with DOX for 1 h, the fluorescence intensity of DOX in the supernatant was reduced compared with the original DOX solution, which indicated the successful loading of DOX onto DNHF. The loading efficiency was calculated to be 78% based on the fluorescence intensity at 590 nm of DOX in the supernatant in comparison with the linear calibration curve of DOX (Figure S21).

Then, the ATP-responsive drug release was monitored after incubation with different concentrations of ATP. As shown in Figure 3C, with the increasing concentration of ATP, the fluorescence intensity of DOX in the supernatants kept rising compared to the control group without ATP treatment, indicating the ATP-responsive drug release for this synthesized DNHFD, which exhibited its potential for specific tumor therapy. Furthermore, the DOX release behavior under varying pH conditions was investigated through incubation with ATP at pH 6.0, 7.4, and 8.0, which displayed similar fluorescence intensity of DOX in the supernatants (Figure S22), demonstrating the sufficient DOX release of this DNA nanohydrogel in different physical environments.

Specificity and Stability of DNA Nanohydrogel. The specificity of DNHFD was investigated by detecting the release of DOX using CTP, GTP, and UTP as controls. After coincubation of DNHFD with ATP, the fluorescence signal exhibited obvious recovery in comparison with the untreated nanohydrogel (Figure 3D), while a negligible increase could be observed for the control group incubated with CTP, GTP, or UTP.

Then, the stability of DNH was verified through monitoring the fluorescence variation after immersing self-quenched DNH in PBS or 10% fetal bovine serum (FBS) buffer for 12 h. As displayed in Figure S23A, the fluorescence intensity of DNH remained relatively steady, indicating the stability of this globular DNA assembly. Additionally, the hydrated diameter of DNH was further monitored through DLS analysis, which exhibited weak variation during 12 h of incubation with PBS or FBS (Figure S23B). These results demonstrated excellent specificity and satisfactory stability of this ATP-responsive DNA nanohydrogel.

Internalization Pathway of DNA Nanohydrogel. Breast cancer is a widely recognized malignant tumor that has emerged as an increasingly significant public health issue in recent years.[32] Therefore, we elected to utilize MCF-7 cells, one of the most commonly employed breast cancer cell lines, to investigate the intracellular characteristics of the designed DNA nanohydrogel. First, the internalization pathway of DNH into MCF-7 cells was assessed using flow cytometric analysis. After pretreatment with various inhibitors (sucrose, genistein, wortmannin, methyl-β-cyclodextrin, and sodium azide) to selectively inhibit specific internalization mechanisms (clathrin-mediated endocytosis, caveolae-mediated endocytosis, macropinocytosis, lipid raft-dependent uptake, and energy-dependent endocytosis, respectively), MCF-7 cells were incubated with fluorescent DNH synthesized by dint of FAM-labeled staple strands to detect the fluorescence detained in cells. As shown in Figure S24, the fluorescence intensity of FAM in MCF-7 cells was significantly attenuated by the addition of sucrose and sodium azide compared to the blank group without any pretreatment, and the suppression rate reached 51% and 35%, respectively. These results provide

https://doi.org/10.1021/acs.analchem.5c00581
Anal. Chem. 2025, 97, 10699−10708

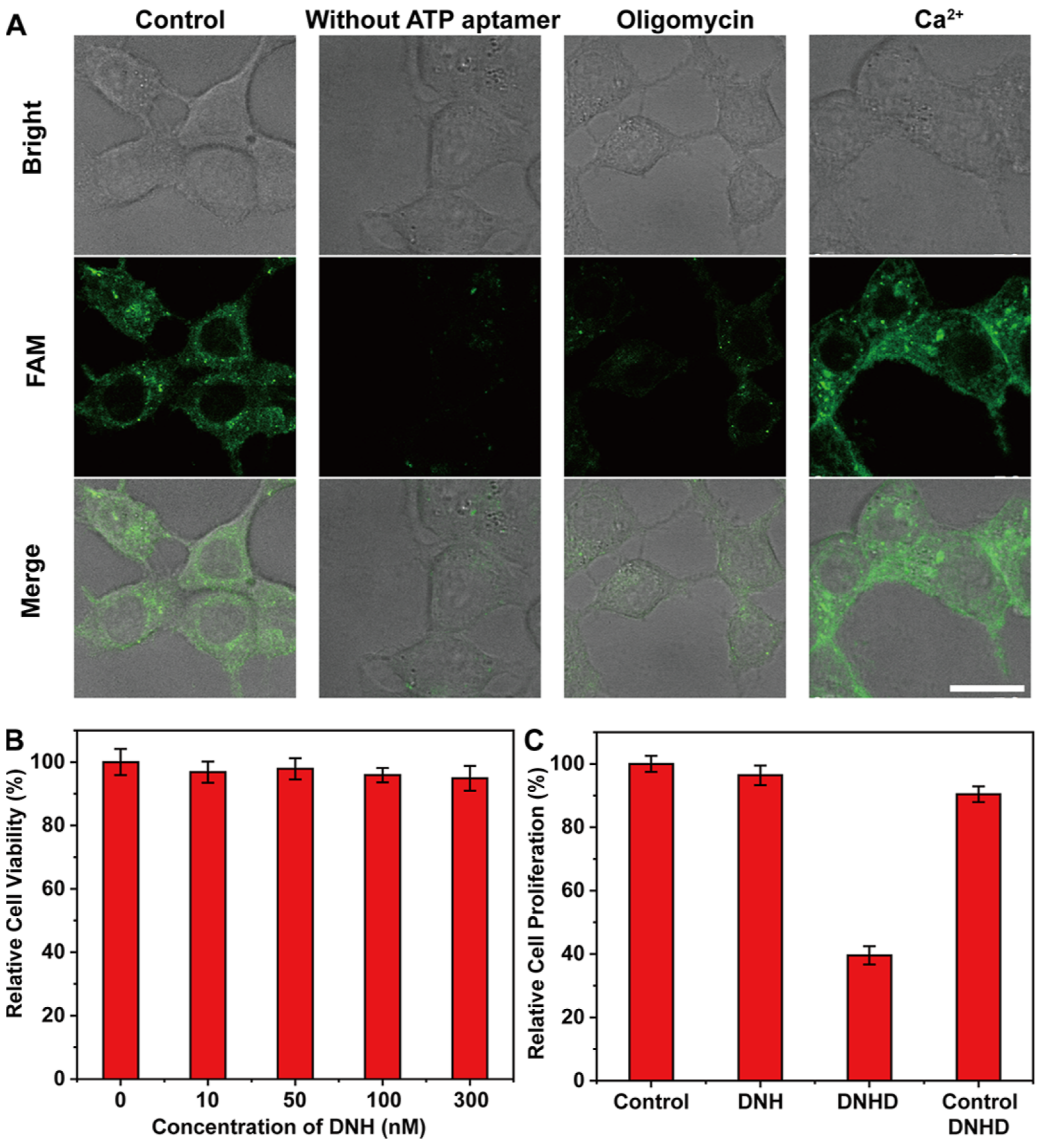

Figure 4. Cell experiment, (A) CLSM images of oligomycin- or Ca^{2+}-pretreated MCF-7 cells incubated with self-quenched DNH or DNH without the ATP aptamer. The scale bar indicates 25 μm. (B) Cell viability of MCF-7 cells treated with different concentrations of DNH. (C) Relative cell proliferation of MCF-7 cells after different treatments. The data error bars indicate means ± SD (n = 3).

evidence that the internalization of DNH primarily occurs through a clathrin-dependent endocytosis pathway in MCF-7 cells.

Fluorescence Validation of ATP Responsiveness in Tumor Cells. The ATP-responsive intracellular imaging was convinced through monitoring the fluorescence recovery of self-quenched DNH in MCF-7 cells with different treatments. After the addition of the ATP inhibitor oligomycin, a weaker fluorescence signal of DNHF could be observed compared to the control group without pretreatment (Figure 4A), whereas the addition of the ATP promoter Ca^{2+} generated intense fluorescence recovery. Additionally, control DNA nanohydrogel without sequences of the ATP aptamer was synthesized using a template with random sequences, which did not induce an observable fluorescence signal of FAM. This reliable ATP responsiveness suggests that the designed DNA nanohydrogel can effectively utilize ATP as a biochemical trigger for tumor-specific responses.

Afterwards, the fluorescence recovery of different cells was examined through flow cytometric analysis to further verify the tumor cell specificity (Figure S25). Normal cells MCF-10A with deficient ATP expression were utilized as a control, which displayed a weaker fluorescence signal, which can be attributed to the higher content of ATP in the tumor cells, while obvious fluorescence recovery of self-quenched DNH could be easily observed in tumor cells (4T1 cells, MCF-7 cells, and MDA-MB-231 cells), indicating the ability for tumor-specific recognition and imaging of this DNA nanohydrogel.

Biosafety and Tumor Cell Therapy of DNA Nanohydrogel. The 3-(4,5-dimethylthiazol-2-yl)-2-diphenyltetrazolium bromide (MTT) cytotoxicity assay was used to evaluate the biocompatibility and biosafety of this DNA nanohydrogel. After incubating with different concentrations of DNH for 6 h, the MCF-7 cells kept a high viability of over 90% in the absence of NIR light exposure (Figure 4B). This result indicates that the DNA nanohydrogel has satisfactory biocompatibility and is not toxic in the absence of DOX. The MTT assay was also used to study the cellular therapeutic efficacy of DOX-loaded DNA nanohydrogel (DNHD). DNHD was incubated with MCF-7 cells for 6 h and then replaced with

https://doi.org/10.1021/acs.analchem.5c00581
Anal. Chem. 2025, 97, 10699−10708

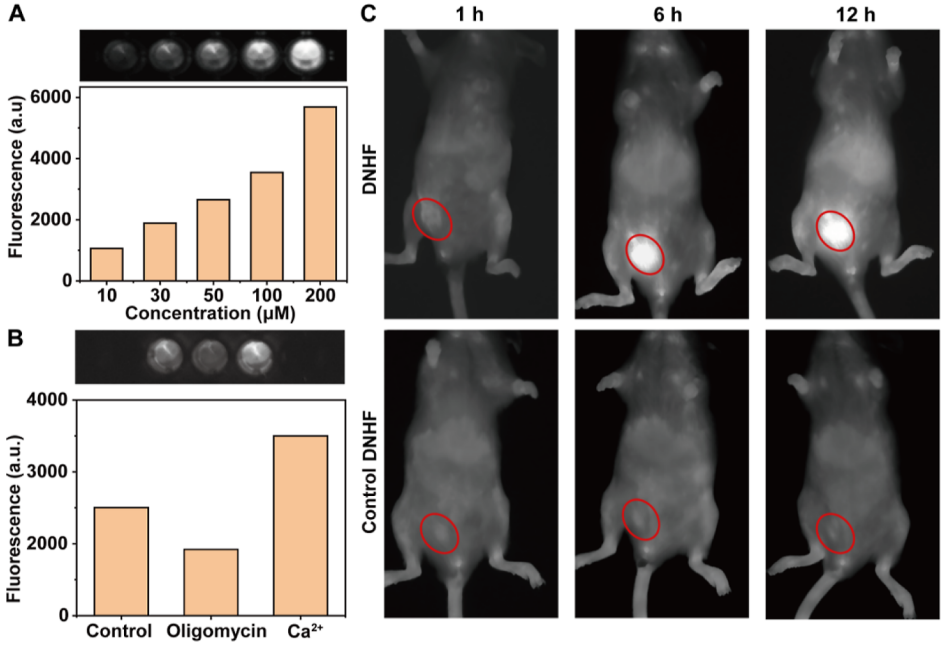

Figure 5. NIR-II fluorescence imaging in cells and in vivo. NIR-II fluorescence images and corresponding intensity values of MCF-7 cells treated with (A) different concentrations of DNHF and (B) 50 μM DNHF along with oligomycin or Ca^{2+} under 808 nm excitation. (C) NIR-II fluorescence imaging of mice bearing breast cancer after treatment with DNHF under 808 nm excitation.

fresh medium containing 10% FBS for another 24 h to assess the cell proliferation rate. As shown in Figure 4C, the cells incubated with DNH exhibited a high proliferation rate of up to 96%, while the DNHD-treated MCF-7 cells caused significant inhibition of cell proliferation (39%), demonstrating the effective tumor cell killing of the DOX-loaded DNA nanohydrogel. For the group without ATP aptamer sequences (control DNHD), the cell proliferation rate kept a high level over 90%, which proved the ATP responsiveness of DOX release and tumor-targeted therapy.

Intracellular NIR-II Fluorescence Imaging. The feasibility of FD-AL-modified DNA nanohydrogel (DNHF) for NIR-II fluorescence imaging of the tumor was first verified through MCF-7 cells. After incubation with the synthesized DNHF for 6 h, MCF-7 cells exhibited an obvious fluorescence signal under 808 nm excitation (Figure 5A). As the concentration of DNHF increased, brighter fluorescence could be collected through a 1000 nm long-pass (LP 1000) filter (Figure 5A), demonstrating the concentration-dependent NIR-II fluorescence performance of this FD-AL-modified DNA nanohydrogel. Afterwards, the ATP inhibitor oligomycin and promoter Ca^{2+} were employed to verify the ATP responsiveness. As shown in Figure 5B, the fluorescence signal became weaker in the cells treated with oligomycin compared to those without pretreatment under incubation with DNHF, while the NIR-II fluorescence became stronger after the addition of Ca^{2+}. These results indicated the ATP-responsive fluorescence enhancement of this DNHF, suggesting its potential in precise tumor NIR-II fluorescence imaging.

In Vivo NIR-II Fluorescence Imaging. The NIR-II fluorescence imaging of the DNA nanohydrogel for early tumor in vivo was examined using mice bearing dimethylbenzanthracene-induced breast cancer. After intravenous injection with the FD-AL-labeled DNA nanohydrogel (DNHF), the NIR-II fluorescent signal of FD-AL from the tumor site became increasingly distinct over time and exhibited a pronounced brightness at 6 h, indicating the efficacy of DNHF for NIR-II fluorescent tumor imaging. Furthermore, the fluorescent signal maintained its brightness even at 12 h after injection, demonstrating the excellent photostability of this NIR-II fluorescent probe (Figure 5C). In the control group treated with control DNHF synthesized without ATP aptamer sequences, the fluorescence at the tumor site was markedly weak, confirming the responsiveness of DNHF to highly expressed ATP in tumors.

To evaluate the in vivo toxicity of the DNA nanohydrogel, major organs in the mice treated with DNHF were collected and sliced for histopathological analysis through hematoxylin and eosin staining. As displayed in Figure S26, the organs in the DNHF group did not exhibit obvious pathological abnormality compared to the control group treated with saline, indicating the satisfactory biocompatibility of this NIR-II fluorescent DNA nanohydrogel. Moreover, the biochemistry analysis of blood in the mice treated with DNHF was conducted through monitoring the blood parameters, including white blood cells (WBCs), red blood cells (RBCs), hematocrit (HCT), hemoglobin concentration (HGB), mean corpuscular hemoglobin (MCH), and platelets (PLT). As shown in Figure S27, the mice with DNHF treatment did not exhibit obvious abnormalities in comparison with the control group treated with saline, indicating the good hemocompatibility and biosafety of the designed DNA nanohydrogel.

The biosafety of DNA nanohydrogel was further evaluated through hemolysis assays. As shown in Figure S28, the DNA nanohydrogel exhibited little hemolysis, and even the DOX-loaded DNA nanohydrogel maintained a low hemolysis ratio below 5%, which was significantly lower than the group treated with free DOX. These results confirmed the outstanding biosafety of the proposed DNA nanohydrogel and further demonstrated its controllability for drug loading and on-demand release.

https://doi.org/10.1021/acs.analchem.5c00581
Anal. Chem. 2025, 97, 10699−10708

CONCLUSIONS

In this study, we have developed a universally adaptable stimulus-responsive nanohydrogel with a simple design for early tumor diagnosis and treatment. The stimuli-responsive conformational switching was realized through the integration of functional DNA modules into long single DNA skeletons, which were synthesized from rolling circle amplification. The bent staple strands modified with FD-AL at both ends facilitated the formation of a spherical structure and induced the quenching effect of NIR-II fluorescence, which could be recovered after the binding with the target. The in vitro experiments verified the "turn-on" NIR-II fluorescence, and the tumor imaging in the mice bearing dimethylbenzanthracene-induced breast cancer indicated the feasibility of this DNA nanohydrogel for early tumor diagnosis. Moreover, the anticancer drug DOX incorporated in the DNA double helix could be effectively released following the disassembly of DNA nanohydrogel, suggesting its application potential in targeted drug delivery and tumor therapy. This design achieved convenient sequence adjustment and superior adaptability for various targets, advancing more opportunities for DNA nanotechnology for commercialization and clinical applications in the field of tumor diagnosis and precise medicine.

EXPERIMENTAL SECTION

ATP Responsiveness Validation. The ATP aptamer chain (2 μL, 10 μM) was taken and reacted with the LS chain (2 μL, 10 μM) in a 20 μL system with a buffer solution of 1 × PBS containing 300 mM Na^+. The DNA strands were annealed at 95 °C for 5 min and then slowly cooled down to room temperature, followed by the addition of concentrations of ATP (1 μM, 3 μM, 5 μM) and incubated at 37 °C for 2 h. A 15% polyacrylamide gel was prepared, and the polyacrylamide gel was placed in an electrophoretic cell containing a 1 × TBE buffer at 100 V for 90 min. The template chain (2 μL, 10 μM) was taken and reacted with the LS chain (2 μL, 10 μM) in 20 μL of buffer solution. The samples were also annealed and added with different concentrations of ATP (1 μM, 5 μM, 10 μM, 50 μM, 100 μM) to incubate at 37 °C for 2 h. A 15% polyacrylamide gel was prepared, and the polyacrylamide gel was placed in an electrophoretic cell containing 1 × TBE buffer at 100 V for 90 min.

LS Chain Folding Validation. The template was annealed with equal concentrations of $LS_{BHQ1/FAM}$ chains modified with BHQ1 and FAM at both ends, respectively. After annealing, different concentrations of ATP (0.1 μM, 0.5 μM, 1 μM, 5 μM, 10 μM) were added, and the fluorescence intensity was measured under an enzyme counter after the reaction for 2 h at 37 °C in a water bath.

Synthesis of RCA. The p-linear (4 μL, 100 μM) was taken with ligation DNA (4 μL, 100 μM), and the reaction was carried out at 95 °C for 5 min and then slowly cooled to room temperature. Then, T4 ligase (1 μL, 400 U/μL) with corresponding buffer (2 μL) was added to react at 25 °C for 16 h and then heated at 65 °C for 10 min to inactivate T4 ligase. After inactivation, ExoI and ExoI buffer and ExoIII and ExoIII buffer were added to the solution, and after reacting at 37 °C for 4 h in a water bath, the exonuclease was inactivated by heating at 85 °C for 15 min to make a DNA cyclic template. 8 μL of the above cyclic template was taken and reacted with a DNA primer (8 μL, 10 μM) in a water bath at 95 °C for 5 min and then slowly cooled to 37 °C. 10 μL of the above solution was taken, and dNTPs (2 μL, 0.1 mM), BSA (1 μL, 0.4 μg/μL), and phi29 DNA polymerase (1 μL, 0.2 U) were added with corresponding buffer (2 μL), and the RCA product was prepared by reacting in a 37 °C water bath for 4 h and then heating at 65 °C for 10 min to inactivate phi29 DNA polymerase.

Synthesis and Validation of DNA Nanohydrogel. DNA nanohydrogels were made by reacting the synthesized RCA long single strand with the modified $LS_{BHQ1/FAM}$ strand at both ends in 1:15. The synthesized nanohydrogels were then measured for fluorescence changes to verify the conformational changes, after which the DNA nanohydrogels were measured by DLS and TEM to detect their morphology. The specific synthetic route of alkyne-modified FD-AL is shown in the Supporting Information. Fluorescent material-modified LS strand was prepared, and the azide-based modified DNA strand was mixed with alkyne-based modified FD-AL at a concentration ratio of 1:10. The reaction was carried out under the action of catalysts copper sulfate and sodium ascorbate at 50 °C for 24 h. At the end of the reaction, extraction was carried out with dichloromethane to remove unreacted FD-AL. After that, DNA nanohydrogels containing fluorescent material FD-AL were prepared according to the above ratio.

The INF-γ-responsive DNA nanohydrogel was prepared with a similar approach except that staple strand-2, linear template-2, primer-2, and ligation DNA-2 were used as substitutions, respectively.

DOX Loading and Validation. DOX loading was performed by mixing 5 μL of DOX (5 mg/mL) with 1 mL of the prepared DNA nanohydrogel to incubate at room temperature for 1.5 h at 37 °C. After centrifugation at 12,000 rpm for 10 min, the supernatant was collected to detect the fluorescence intensity of DOX under 480 nm excitation, and the loading yield was calculated in comparison with the calibration curve of DOX. The different concentrations of ATP (0 μM, 5 μM, 10 μM, 50 μM, 100 μM, 200 μM) were added and incubated for 2 h to detect the fluorescence changes of DOX. After that, the specific release of ATP was detected by incubating with equal concentrations (100 μM) of ATP, CTP, GTP, and UTP, respectively, for 2 h for the detection of fluorescence. DOX-loaded DNHFD was incubated with 100 μM ATP under different pH conditions (6.0, 7.4, 8.0) at 37 °C for 1.5 h to monitor DOX release under varying pH.

Investigation of the Endocytosis Pathway. MCF-7 cells were transfected in 96-well plates for 24 h and then pretreated with sucrose, genistein, wortmannin, methyl-β-cyclodextrin, and sodium azide for 6 h. After incubation with FAM-modified DNA nanohydrogel for 12 h, the cells were washed with PBS three times and collected for the flow cytometric assay over the FL1 channel.

CLSM Imaging and the Flow Cytometry Assay. The intracellular ATP responsiveness was verified using the self-quenched DNA nanohydrogel synthesized from BHQ1- and FAM-labeled $LS_{BHQ1/FAM}$ chains. After pretreatment with oligomycin or Ca^{2+} for 30 min, the MCF-7 cells were incubated with self-quenched DNA nanohydrogel for 6 h to conduct the CLSM fluorescence imaging. The FAM fluorescence signal was collected from 500 to 550 nm under 488 nm excitation. In addition, the DNA nanohydrogel without ATP responsiveness was also synthesized using a long single strand without ATP aptamer sequences to perform as a control. For the fluorescence recovery assay in different cells, four types of cells (4T1 cells, MCF-7, MDA-MB-231, and

https://doi.org/10.1021/acs.analchem.5c00581
Anal. Chem. 2025, 97, 10699−10708

MCF-10a) were selected and incubated with 1 nM self-quenched DNA nanohydrogel for 6 h, respectively, followed by the flow cytometric assay over the FL1 channel to detect the fluorescence recovery assay of FAM.

MTT Detection. For evaluating the biocompatibility of DNA nanohydrogel, MCF-7 cells were incubated with different concentrations of DNHF (0, 10, 50, 100, and 300 nM) for 12 h, and the cellular activity was assayed using the MTT kit. To verify the tumor therapy efficacy of DOX-loaded DNA nanohydrogel, MCF-7 cells were treated with 100 nM DNHF, DNHF loaded with DOX (DNHFD), or control DNHFD without ATP aptamer sequences for 6 h. After washing and incubation with fresh medium for another 24 h, the cellular proliferation rate was detected by an MTT kit (Yeasen, China).

Intracellular NIR-II Imaging. MCF-7 cells with a good growth status were transfected into 96-well plates and incubated for 24 h. Then, 10 μM, 30 μM, 50 μM, 100 μM, and 200 μM of DNHF were added and incubated for 6 h, and the NIR-II fluorescence was recorded under 808 nm excitation. MCF-7 cells were added with oligomycin or Ca^{2+} and incubated for 30 min, followed by the incubation with 50 μM DNHF for 6 h. Then, NIR-II fluorescence imaging was conducted under 808 nm excitation. The intensity of the NIR-II fluorescence signal was collected with a 1000 nm long-pass (LP 1000) filter and measured by ImageJ.

In Vivo NIR-II Imaging. To verify the NIR-II fluorescence imaging ability of DNHF, a 7,12-dimethylbenzanthracene (DMBA)-induced breast cancer model was established in BALB/c mice (5−6 weeks) (Keygen Biotech, China). All procedures during the in vivo experiments were performed in conformity with the Institutional Animal Use and Care Regulations and approved through the Model Animal Research Center in Nanjing University of Chinese Medicine. The mice with breast cancer were randomly divided into three groups and intravenously injected with 150 μL saline, control DNHF without ATP aptamer sequences (1 nM), and DNHF (1 nM). At 6 h after injection, the mice were imaged on the NIR-II In Vivo Imaging System (Series III 900/1700, Suzhou NIR-Optics Technologies Co., Ltd., China). The NIR-II fluorescence imaging was recorded under 808 nm excitation in an in vivo imaging chamber, and the fluorescence signal was collected with a 1000 nm long-pass (LP 1000) filter.

Histopathological Analysis and Biochemistry Analysis. The major organs of mice treated with saline and DNHF were harvested to conduct the histopathological analysis using a hematoxylin and eosin staining kit (Yeasen, China). After fixing with 4% paraformaldehyde, the organs were embedded in paraffin blocks and sliced for hematoxylin and eosin staining according to the manufacturer's instructions, and the sections of organs were then visualized using the optical microscope (Olympus BX51, Japan). The blood samples from mice treated with saline and DNHF were then collected for biochemistry analysis including white blood cells (WBCs), red blood cells (RBCs), hematocrit (HCT), hemoglobin concentration (HGB), mean corpuscular hemoglobin (MCH), and platelets (PLT).

Hemolysis Assay. Blood samples from mice were collected in heparinized tubes. After washing with physiological saline and centrifugation at 3000 rpm for 10 min, the red blood cells (RBCs) were resuspended in PBS to prepare a 2% RBC suspension. 50 μM free DOX, DNA nanohydrogel (DNH), or DOX-loaded DNA nanohydrogel (DNHD) were added, with water and PBS serving as positive and negative controls, respectively. The RBC suspension was incubated under different treatment conditions at 37 °C for 1 h. The supernatant was collected through centrifugation, and the absorbance (OD) at 545 nm was measured to calculate the hemolysis ratio according to the previous reports.[18,33]

■ ASSOCIATED CONTENT

Supporting Information

The Supporting Information is available free of charge at https://pubs.acs.org/doi/10.1021/acs.analchem.5c00581.

Materials, apparatus, cell culture, synthesis of alkyne-modified FD-1080, and additional data (PDF)

■ AUTHOR INFORMATION

Corresponding Authors

Qichen Zhan − *State Key Laboratory of Technologies for Chinese Medicine Pharmaceutical Process Control and Intelligent Manufacture, Nanjing University of Chinese Medicine, Nanjing 210023, China;* orcid.org/0000-0002-3456-0124; Email: zhanqichen@njucm.edu.cn

Peng Cao − *State Key Laboratory of Technologies for Chinese Medicine Pharmaceutical Process Control and Intelligent Manufacture, Nanjing University of Chinese Medicine, Nanjing 210023, China; The Quzhou Affiliated Hospital of Wenzhou Medical University, Quzhou People's Hospital, Quzhou, Zhejiang 324000, China; Clinical Medical Research Center, Zhenjiang Hospital of Chinese Traditional and Western Medicine, Zhenjiang 212004, China;* orcid.org/0000-0002-2044-3074; Email: cao_peng@njucm.edu.cn

Huangxian Ju − *State Key Laboratory of Analytical Chemistry for Life Science, School of Chemistry and Chemical Engineering, Nanjing University, Nanjing 210023, China;* orcid.org/0000-0002-6741-5302; Email: hxju@nju.edu.cn

Yue Zhang − *State Key Laboratory of Technologies for Chinese Medicine Pharmaceutical Process Control and Intelligent Manufacture, Nanjing University of Chinese Medicine, Nanjing 210023, China;* orcid.org/0000-0002-7902-4253; Email: zhangyue035@njucm.edu.cn

Authors

Feng Gao − *State Key Laboratory of Technologies for Chinese Medicine Pharmaceutical Process Control and Intelligent Manufacture, Nanjing University of Chinese Medicine, Nanjing 210023, China*

Lichao Guo − *State Key Laboratory of Technologies for Chinese Medicine Pharmaceutical Process Control and Intelligent Manufacture, Nanjing University of Chinese Medicine, Nanjing 210023, China*

Wanjuan Lin − *State Key Laboratory of Technologies for Chinese Medicine Pharmaceutical Process Control and Intelligent Manufacture, Nanjing University of Chinese Medicine, Nanjing 210023, China*

Xiaobo Zhang − *State Key Laboratory of Analytical Chemistry for Life Science, School of Chemistry and Chemical Engineering, Nanjing University, Nanjing 210023, China;* orcid.org/0000-0003-0222-2515

Complete contact information is available at: https://pubs.acs.org/10.1021/acs.analchem.5c00581

https://doi.org/10.1021/acs.analchem.5c00581
Anal. Chem. 2025, 97, 10699−10708

Author Contributions

[⊥]Feng Gao and Lichao Guo contributed equally to this work. Qichen Zhan provided support for cellular and animal experiments. Peng Cao is responsible for the coordination of experimental design and data analysis. Huangxian Ju provided support for the synthesis of NIR-II fluorescent dye FD-AL and the apparatus for NIR-II fluorescence analysis. Yue Zhang offered guidance in the overall experimental design, manuscript writing, and discussion of results.

Notes

The authors declare no competing financial interest.

■ ACKNOWLEDGMENTS

We gratefully acknowledge the National Key R&D Program of China (2023YFC2308200), the National Natural Science Foundation of China (82125037, 22104063), the Natural Science Foundation of Jiangsu Province, China (SBK2021042488), and Nanjing University of Chinese Medicine (XPT22104063).

■ REFERENCES

(1) Kou, Z.; Zhao, P.; Wang, Z.; Jin, Z.; Chen, L.; Su, B. L.; He, Q. *J. Mater. Chem. B* **2019**, *7* (17), 2759−2765.
(2) Li, Y.; Lin, J.; Wang, P.; Luo, Q.; Lin, H.; Zhang, Y.; Hou, Z.; Liu, J.; Liu, X. *ACS Nano* **2019**, *13* (11), 12912−12928.
(3) Zhang, C.; Ni, D.; Liu, Y.; Yao, H.; Bu, W.; Shi, J. *Nat. Nanotechnol.* **2017**, *12* (4), 378−386.
(4) Zhou, Q.; Shao, S.; Wang, J.; Xu, C.; Xiang, J.; Piao, Y.; Zhou, Z.; Yu, Q.; Tang, J.; Liu, X.; Gan, Z.; Mo, R.; Gu, Z.; Shen, Y. *Nat. Nanotechnol.* **2019**, *14* (8), 799−809.
(5) Wang, Z.; Ju, Y.; Ali, Z.; Yin, H.; Sheng, F.; Lin, J.; Wang, B.; Hou, Y. *Nat. Commun.* **2019**, *10* (1), 4418.
(6) Zheng, M.; Zhao, P.; Luo, Z.; Gong, P.; Zheng, C.; Zhang, P.; Yue, C.; Gao, D.; Ma, Y.; Cai, L. *ACS Appl. Mater. Interfaces* **2014**, *6* (9), 6709−6716.
(7) Huang, Y.; Wei, D.; Wang, B.; Tang, D.; Cheng, A.; Xiao, S.; Yu, Y.; Huang, W. *Acta Biomater.* **2023**, *160*, 198−210.
(8) Pourhajibagher, M.; Etemad-Moghadam, S.; Alaeddini, M.; Miri Mousavi, R. S.; Bahador, A. *Sci. Rep.* **2022**, *12* (1), 12161.
(9) Hendrikse, S. I. S.; Gras, S. L.; Ellis, A. V. *ACS Nano* **2019**, *13* (8), 8512−8516.
(10) Wang, P.; Wang, X.; Luo, Q.; Li, Y.; Lin, X.; Fan, L.; Zhang, Y.; Liu, J.; Liu, X. *Theranostics* **2019**, *9* (2), 369−380.
(11) Zhang, M.; Yue, J.; Cui, R.; Ma, Z.; Wan, H.; Wang, F.; Zhu, S.; Zhou, Y.; Kuang, Y.; Zhong, Y.; Pang, D. W.; Dai, H. *Proc. Natl. Acad. Sci. U.S.A.* **2018**, *115* (26), 6590−6595.
(12) Yang, Q.; Hu, Z.; Zhu, S.; Ma, R.; Ma, H.; Ma, Z.; Wan, H.; Zhu, T.; Jiang, Z.; Liu, W.; Jiao, L.; Sun, H.; Liang, Y.; Dai, H. *J. Am. Chem. Soc.* **2018**, *140* (5), 1715−1724.
(13) Liu, Y.; Li, Y.; Koo, S.; Sun, Y.; Liu, Y.; Liu, X.; Pan, Y.; Zhang, Z.; Du, M.; Lu, S.; Qiao, X.; Gao, J.; Wang, X.; Deng, Z.; Meng, X.; Xiao, Y.; Kim, J. S.; Hong, X. *Chem. Rev.* **2022**, *122* (1), 209−268.
(14) Li, X.; Jiang, M.; Li, Y.; Xue, Z.; Zeng, S.; Liu, H. *Mater. Sci. Eng., C* **2019**, *100*, 260−268.
(15) Mandal, A. K.; Wu, X.; Ferreira, J. S.; Kim, M.; Powell, L. R.; Kwon, H.; Groc, L.; Wang, Y.; Cognet, L. *Sci. Rep.* **2020**, *10* (1), 5286.
(16) Zhong, Y.; Ma, Z.; Wang, F.; Wang, X.; Yang, Y.; Liu, Y.; Zhao, X.; Li, J.; Du, H.; Zhang, M.; Cui, Q.; Zhu, S.; Sun, Q.; Wan, H.; Tian, Y.; Liu, Q.; Wang, W.; Garcia, K. C.; Dai, H. *Nat. Biotechnol.* **2019**, *37* (11), 1322−1331.
(17) Zhang, Z.; Fang, X.; Liu, Z.; Liu, H.; Chen, D.; He, S.; Zheng, J.; Yang, B.; Qin, W.; Zhang, X.; Wu, C. *Angew. Chem., Int. Ed.* **2020**, *59* (9), 3691−3698.
(18) Xu, Y.; Li, C.; Lu, S.; Wang, Z.; Liu, S.; Yu, X.; Li, X.; Sun, Y. *Nat. Commun.* **2022**, *13* (1), 2009.
(19) Li, C.; Tu, L.; Xu, Y.; Li, M.; Du, J.; Stang, P. J.; Sun, Y.; Sun, Y. *Angew. Chem., Int. Ed.* **2024**, *63* (37), No. e202406392.
(20) Xu, Y.; Li, C.; An, J.; Ma, X.; Yang, J.; Luo, L.; Deng, Y.; Kim, J. S.; Sun, Y. *Sci. China: Chem.* **2023**, *66* (1), 155−163.
(21) Pan, W. L.; Tan, Y.; Meng, W.; Huang, N. H.; Zhao, Y. B.; Yu, Z. Q.; Huang, Z.; Zhang, W. H.; Sun, B.; Chen, J. X. *Biomaterials* **2022**, *283*, 121449.
(22) Kazemi, Y.; Dehghani, S.; Soltani, F.; Abnous, K.; Alibolandi, M.; Taghdisi, S. M.; Ramezani, M. *Nanomed. Nanotechnol. Biol. Med.* **2022**, *45*, 102588.
(23) Chen, K.; Zhang, Y.; Zhu, L.; Chu, H.; Shao, X.; Asakiya, C.; Huang, K.; Xu, W. *J. Controlled Release* **2022**, *341*, 869−891.
(24) Jiang, L.; Chen, H. Y.; He, C. H.; Xu, H. B.; Zhou, Z. R.; Wu, M. S.; Fodjo, E. K.; He, Y.; Hafez, M. E.; Qian, R. C.; Li, D. W. *Anal. Chem.* **2023**, *95* (6), 3507−3515.
(25) Kenry; Duan, Y.; Liu, B. *Adv. Mater.* **2018**, *30* (47), No. e1802394.
(26) Fang, Y.; Yan, Y.; Bi, S.; Wang, Y.; Chen, Y.; Xu, P.; Ju, H.; Liu, Y. *Anal. Chem.* **2022**, *94* (38), 13205−13214.
(27) Li, Y.; Xie, Y.; Zhang, Y.; Zhao, H.; Ju, H.; Liu, Y. *Anal. Chim. Acta* **2022**, *1221*, 340149.
(28) Jin, Y.; Wang, H.; Li, X.; Zhu, H.; Sun, D.; Sun, X.; Liu, H.; Zhang, Z.; Cao, L.; Gao, C.; Wang, H.; Liang, X. J.; Zhang, J.; Yang, X. *ACS Appl. Mater. Interfaces* **2020**, *12* (24), 26832−26841.
(29) Cheng, Q.; Tian, Y.; Dang, H.; Teng, C.; Xie, K.; Yin, D.; Yan, L. *Adv. Healthcare Mater.* **2022**, *11* (1), No. e2101697.
(30) Mei, J.; Leung, N. L.; Kwok, R. T.; Lam, J. W.; Tang, B. Z. *Chem. Rev.* **2015**, *115* (21), 11718−11940.
(31) Li, H.; Kim, H.; Xu, F.; Han, J.; Yao, Q.; Wang, J.; Pu, K.; Peng, X.; Yoon, J. *Chem. Soc. Rev.* **2022**, *51* (5), 1795−1835.
(32) BioMed Research International. *BioMed Res. Int.* **2023**, *2023*, 9872034.
(33) Zhang, C.; Wu, J.; Liu, W.; Zhang, W.; Lee, C. S.; Wang, P. *Acta Biomater.* **2023**, *159*, 247−258.

https://doi.org/10.1021/acs.analchem.5c00581
Anal. Chem. 2025, 97, 10699−10708